

Simulation and Estimation of Intracellular Dynamics and Trafficking

Jérôme Boulanger, Thierry Pécot, Patrick Bouthemy, Jean Salamero, Jean-Baptiste Sibarita, and Charles Kervrann

In this chapter, we present an original modeling framework for membrane trafficking modeling and video-microscopy. Understanding the complexity of cellular processes requires a better knowledge of their dynamic properties and geometric structures. Over the last decade, progresses in cellular and molecular biology as well as in microscopy allow cell visualization while acquiring multidimensional data of their fastly occurring activities.

The proposed method is devoted to the analysis of the dynamical content of microscopy image sequences corresponding to dynamical events related to membrane transport. This chapter is organized as follows. In Section 7.1, the major biological issues are introduced, as well as the optical instruments used for investigation. In this chapter, video-microscopy reveals the dynamical behavior of tagged proteins within the living cell. To capture the movements of these proteins, we propose new models to mimic trafficking of proteins within the cell by making the analogy with computer networks or road networks (Section 7.2). In addition, we provide a framework for *simulating* the foreground and background components observed in real image sequences. Section 7.3 is dedicated to the estimation of the background model. In Section 7.4, we consider the problem of estimating the origin-destination probabilities of the tagged proteins for the trafficking network.

7.1 Context

To guarantee the structure, cohesion, and functions of the organism, the eukariotic cell exchanges information between its compartments and organelles: endosomes, Golgi apparatus, and endoplasmic reticulum (ER), and so on. These intracellular exchanges require physical supports or networks for communication. Transportation of molecules from a donor compartment to an acceptor compartment is actually guided by the cell cytoskeleton made of actin filaments, intermediate filaments, and microtubules. The interactions of membranes with microtubules are mediated by several classes of proteins, notably motor proteins of the dynein and kinesin families. The involvement of these motors in the dynamics of various organelles including transport intermediates and cellular structures along microtubules is now well established. In our study, the transport intermediates corresponding to small spherical vesicles move along these “rails”—that is, the microtubules organized by the centrosome (see Figure 7.1). The molecular motors transform the ATP energy

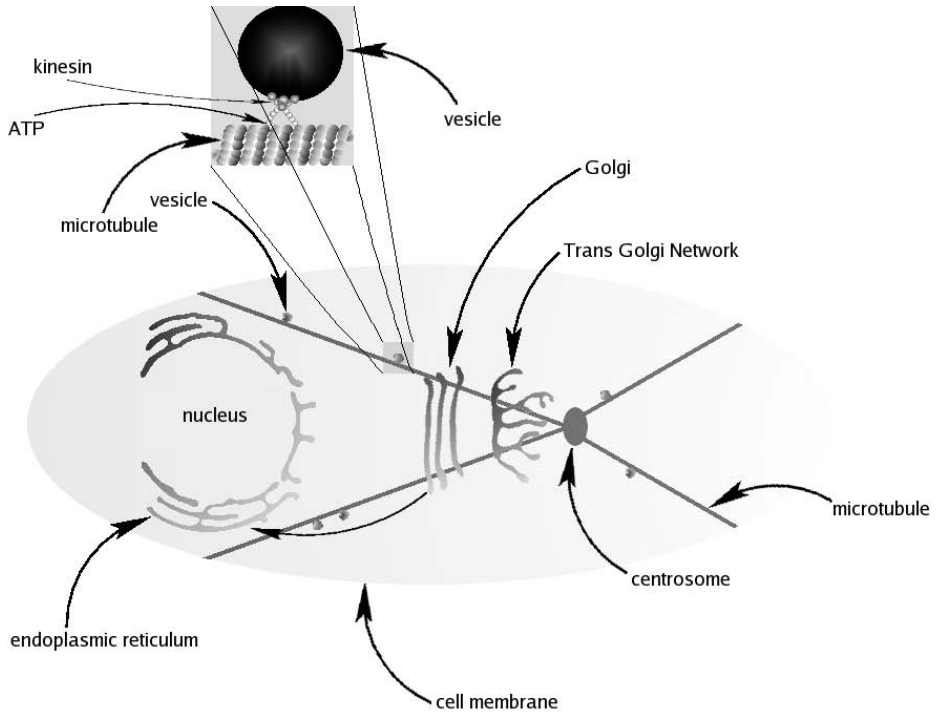


Figure 7.1 Cell compartments and organelles involved in our study.

produced into a driving energy either in the polymerization direction (e.g., kinesin) or in the depolymerization direction (e.g., dynein) of microtubules, also in action. In what follows, we will assume that the velocities of microtubules is relatively low when compared to the velocities of vesicles.

7.1.1 Introduction to Intracellular Traffic

In eukaryotic cells, the constant dynamic process ensuring the steady state distribution of membrane resident proteins and maintaining a balance in the lipid composition of the internal membranes is tightly regulated by a number of proteins. Among these proteins, some are members of the family of Rab-GTPases that bind reversibly to specific membranes within the cells. It is established that the GTPases of the Rab family (about 60 members for human cells) are responsible for the recruitment of proteins that form the vesicles. In this chapter, we will focus on the traffic between the Golgi apparatus and ER, presumably regulated by two isoforms of the Rab6-GTPase, Rab6A and Rab6A', which differ in only a few amino acids. Rab6 is suspected to select among the set of molecular motors those that are the more appropriate for moving molecules to their final destinations in an intracellular compartment. It is now established that Rab6A defines a novel retrograde pathway that is the flux of proteins and lipids from the Golgi apparatus to the ER. More precisely, Rabkinesin-6, a Golgi-associated kinesin-like protein

that only interacts with Rab6A, could be involved in the movement of retrograde transport intermediates between Golgi and ER, but this function is still a matter of controversy. This pathway is also used by certain toxins to reach ER.

We visualized a fluorescent-protein (FP) fusion to Rab6, a Golgi-associated GTPase. Observation of protein dynamics in live cells using fusions to the green fluorescent protein (GFP) and video-microscopy (Fast 4D deconvolution microscopy) enables us to clarify the respective role of Rab6A and Rab6A' in retrograde transport. Thanks to the technological developments performed by the imaging facilities team of the UMR 144 and the Institut Curie, fast dynamics of FP-Rab6 in living cells can be captured in 3-D. We observe that Rab6A mainly associates with the cytosolic face of the Golgi apparatus. Cellular dynamics of Rab6A should be influenced by at least three distinct phenomena: (1) lateral diffusion dictated by lipid movement within a continuum of membranes, (2) continuous exchange between cytosolic and membrane bound pools, and (3) directional motion on membrane transport intermediates. While Rab6A-GFP is concentrated on the cytosolic face of the Golgi membranes, it also associates with rapidly moving transport intermediates that are believed to reach particular stable structures or vesicular clusters located at the cell periphery and referred as end points or ER entry points.

7.1.2 Introduction to Living Cell Microscopy

Light microscopy provides cell biologists with the unique possibility of monitoring living samples in their native state. Thanks to recent progress in cellular biology, molecular biology, and microscopy, it is now feasible to observe the cellular activities of various organelles within the cell, in three dimensions, at high spatial and temporal resolutions. These observations are achieved by means of optical sectioning microscopy, in which images are recorded while the focal plane is rapidly and precisely raised through the sample. The three-dimensional (3-D) acquisition process is repeated at several time points during a given period, leading to the collection of image stacks in four dimensions (4-D). The introduction of natural fluorescent probes such as green fluorescent protein (GFP), combined with the increase in the sensitivity of high-resolution detectors, have made it possible to observe living cells for a long period of time at low light excitation levels. It is now routinely possible to collect images of living cells at up to 30 frames per second at optical resolution without disturbing the cell activity. In most intracellular trafficking studies, the optical resolution of wide-field microscopy, which is in the range of the wavelength of light used, is not sufficiently high to optically resolve the organelles of interest. Together with the need for acquisition speed and low light excitation level, they result in blurring and noise, making the data difficult to analyze. Confocal microscopes provide higher spatial resolution in the axial direction, but it is at the expense of loss of precious photons in the detection side. Considering speeds and spatial distribution of organelles taking part in the membrane trafficking, and more especially in the case of Rab6A proteins, we have chosen to perform data acquisition using rapid 4-D wide-field microscopy combined with deconvolution. Actually, part of this protein is carried through a large number of vesicles moving at speeds reaching up to few microns per second in three dimensions. Nevertheless, even

with this rapid technique and the use of image restoration process, the collected images remain difficult to analyze by traditional image analysis methodologies.

Image processing methods have already been developed to reliably track the vesicles over time, with promising results. The computed trajectories can then be used to evaluate trafficking (orientation, velocities, and so on). In this chapter, we propose an alternative and global approach, motivated by actors and components “in motion.” This investigation is of major importance since supervising and/or controlling traffic means that appropriate drugs could be used to either better regulate or limit communication between compartments. The proliferation of cancerous cells could be potentially controlled by stopping molecule transportation.

7.2 Modeling and Simulation Framework

In this section, we present the modeling and a simulation approach for intracellular membrane trafficking. We first introduce the computational model and then provide a method to simulate microscopy image sequences and applications.

7.2.1 Intracellular Trafficking Models in Video-Microscopy

Two kinds of approaches have been mainly investigated for modeling image sequences: *data-driven modeling* and *physics-based modeling*. Physics-based approaches exploit physical properties of the scene and optical characteristics of imaging systems to set up an image model. The main advantage relies on the fact that model parameters are given by physics. Hence, they directly correspond to the real world as explained in [1,2] and can be thus easily interpreted. It is worth noting that the complexity of scenes and models is usually an obstacle to this approach, and the *inverse problems* related to the estimation parameters are severely “ill-posed.” *Data-driven modeling* aims at describing image sequences through statistical models learned from real images [3]. This approach is used to mimic a set of dynamical processes occurring frequently in real image sequences, but is not able to describe the physical properties of real processes. *Data-driven* and *physics-based* approaches can be also combined to describe the main components of the image sequences. In video-microscopy and GFP-tagging, these components are essentially the moving objects (foreground), the slowly varying cytosol (background), and some noise due to the acquisition system. Figure 7.2 illustrates this decomposition into background and foreground components. In this section, we propose models for these two components.

7.2.1.1 Background Modeling in Video-Microscopy

In images sequences, large structures and compartments within the cell like the Golgi apparatus and the cytosol appear as nearly static during the observation time interval. In the case of images showing fluorescently tagged particles, the global image intensity is proved to vary slowly along time. This can be due to several physical phenomena, such as photobleaching or diffusion of fluorescent proteins within the cell. Therefore, it is appropriate to propose a model able to describe

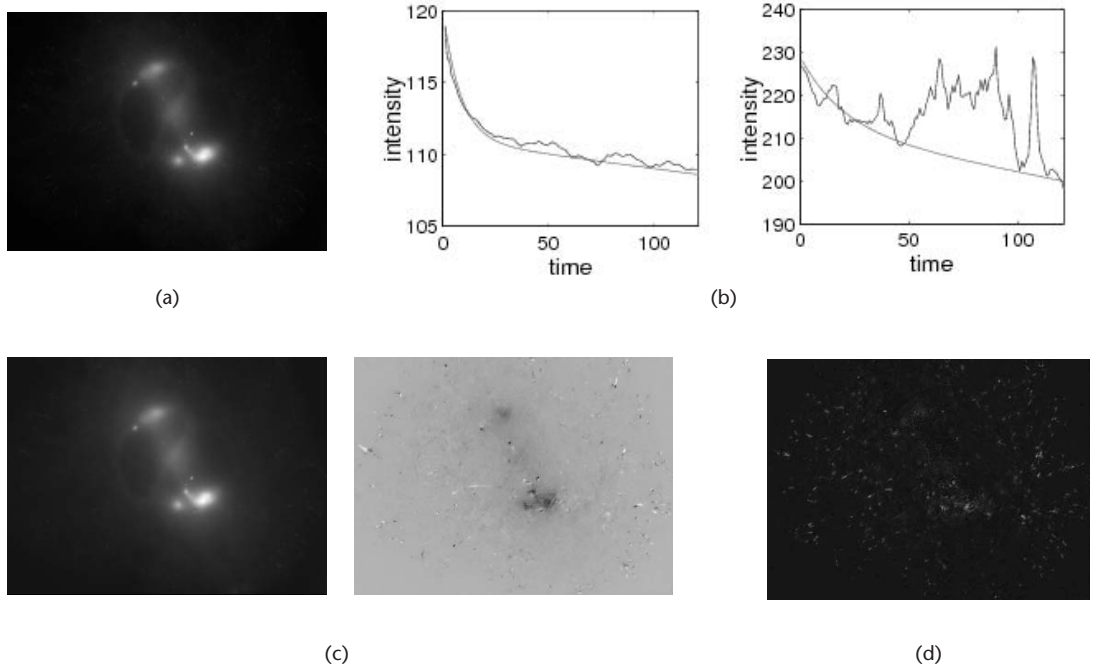


Figure 7.2 (a) GFP-tagging microscopy image. (b) Temporal intensity signals for two different pixels of the image (a). (c) The two components of the background of the image (a). (d) Foreground of the image (a).

the slowly spatially and temporally varying background, since a stationary model would be too restrictive. The modeling of moving small objects corresponding to transport intermediates with variable velocities will be addressed in Section 7.3.

First, we have conducted experiments showing that the intensity variation with respect to time can be captured by a linear model for each pixel of the image sequence, mainly because we are dealing with sequences of limited length. This crude modeling provides a compact representation of the background, described by two 2-D maps corresponding to the two spatially varying parameters. Nevertheless, these parameters are spatially correlated, which must be taken into account later in the estimation process. Note that the proposed approach is general and valid for polynomial models and/or exponential forms if required. Formally, we propose the following image sequence model for the background:

$$f_i(t) = a_i + b_i t + u_i(t) + \varepsilon_i(t) \quad (7.1)$$

where $f_i(t)$ denotes the intensity observed at pixel $p_i = (x_i, y_i)^T$ and time t , and the two coefficients a_i and b_i vary with the spatial image position p_i . The function $u_i(t)$ is a positive function that describes the intensity of moving intermediate transports (or vesicles) if any, and $\varepsilon_i(t)$ is the error term assumed to be described by an additive white Gaussian noise. This model is able to describe the background intensity of the whole image sequence with only two 2-D maps $\{a_i\}$ and $\{b_i\}$, whose size is

equal to the size of each image extracted from the temporal sequence. Section 7.3 proposes a statistical method to estimate both the maps $\{a_i\}$ and $\{b_i\}$.

7.2.1.2 Intracellular Membrane Trafficking Modeling

Acquired image sequences contain small bright and fast moving blobs superimposed against slowly varying background. These objects indicate the location of tagged proteins bounded to vesicle membranes. By using these transport intermediates, molecules are passed from a donor compartment to an acceptor compartment.

A simple and commonly adopted model to represent these blobs is a 2-D Gaussian function whose standard deviation is related to the size of the blob. Theoretically, the object diameters range from 60 nm to 150 nm, and the resolution of the microscope is about $200 \times 200 \times 500$ nm. Accordingly, the diameter of blobs is expected to be below this spatial resolution. However, the point spread function of the video-microscope makes them appear as larger structures even if a deconvolution process is applied [4]. Furthermore, when the density of objects increases, vesicles gather together and constitute small aggregates or rods [5].

These objects are also known to move along microtubules (i.e., along elongated protein polymers that have an exceptional bending stiffness). Microtubules are conveyor belts inside the cells. They drive vesicles, granules, organelles like mitochondria, and chromosomes via special attachment proteins using molecular motors. It is established that molecular motors form a class of proteins responsible for the intracellular transport within the cells. The dynein and kinesin proteins are two different motors associated with microtubules. We consider in our study that in stable conditions, the speed of these motors is constant. This mainly explains why the observed velocity of vesicles is approximately constant if they move along the same microtubule [6].

Vesicles use a microtubule network to carry molecules from a donor compartment to an acceptor compartment (i.e., from the Golgi apparatus to the endoplasmic reticulum). Accordingly, instead of brownian motion or random walks for the vesicles, we consider directed walk models and associated statistical graphs. Hence, each origin vertex and destination vertex of the graph are specific sites on the microtubule network. In addition, once origin-destination pairs have been defined, paths between two vertices are computed according to a routing mechanism. Each object follows a preferential path to reach its target destination. The so-called “origin-destination modeling” is a key point of the proposed framework and is related to the concept of network tomography, as the proposed framework and is related to the concept of network tomography, as we shall see in Section 7.4.

7.2.2 Intracellular Traffic Simulation

7.2.2.1 Motivations

In many application fields such as medical imaging or astronomy, simulations are required for validating physical models and understanding recorded data. We give the rationale behind the idea of simulation methods for video-microscopy.

First, realistic simulations of dynamical processes usually give a qualitative representation of the observed spatio-temporal biological events. Simulation can then be considered as a computational tool useful for understanding some mechanisms of internal components within the cell. Then, by interacting with the control parameters, an expert can artificially generate processes of the real world provided the underlying dynamical models are known; this philosophy has been successfully exploited to understand dynamics of microtubule networks [7,8]. By modeling two sets of descriptors respectively computed from a real image sequence and a simulated sequence using an optimization procedure, artificial data can be computed. The set of estimated control parameters can be then considered as a parsimonious representation of the underlying process.

Moreover, simulated image sequences constitute a set of ground truths that can be exploited to measure the performance of object detection, object tracking, and optical flow algorithms [9,10]. Benchmarking data sets are necessary to get reference data and are now widely used in computer vision to evaluate image analysis algorithms [11,12]. Most of image processing tasks cannot be done manually, and they must be fast, reliable, and reproducible. In biomedical imaging, simulation of ground truths is also a crucial and challenging problem. Thus realistic benchmarks have to be generated for each target application.

Simulation methods must be *controllable* [13] with a limited number of parameters. In most cases, the parameters are related not only to the physical properties of the system, but also to the properties of the objects of interest observed in the image, such as scale and velocity. By using a representation with a few degrees of freedom, the simulation method becomes more interactive and intuitive, and allows the expert to bring some a priori knowledge or to plan a set of experiments by editing the simulation. In our case, the expert specifies the locations of origin and destination for the moving objects and then modifies traffic statistics. At last, the expert feedback can be used to set up a realistic simulation.

7.2.2.2 Background Simulation

In our study, the background model associated with the cytosol and other static organelles is described by two 2-D maps $\{a_i\}$ and $\{b_i\}$. These maps can be estimated from acquired data using the procedure described in Section 7.3 or given a priori. Typically, a completely synthetic example can also be obtained by setting the first and the last frame of the sequence corresponding to the background.

7.2.2.3 Membrane Trafficking Simulation

Foreground components are generated using a four-step approach. First, the network is extracted from a real image sequence or provided by a user. Then, the origin-destination pairs are selected, and the paths between the corresponding nodes are computed in a third step. Finally, we simulate moving vesicles and trains/aggregates from computed locations and paths. In the following, this procedure is described in detail.

Network Extraction

For a trafficking simulation, a microtubule network must be first computed. At first glance, we could exploit the self-organization properties of the microtubule network and try to simulate data as already proposed in [8,14]. Based on the interaction between the motors (e.g., kinesine) and microtubules, the author describes some characteristic conformations such as mitotic spindle. However, even if the approach is attractive, this computer simulation describes only the behavior of the microtubule network *in vitro*; it is not adapted for the more complex *in vivo* case in which the microtubules interact with other organelles of the cell. To produce a synthetic but realistic microtubule network, we decide to use real image sequences as input data for modeling. In what follows, the microtubule network is crudely computed from a maximum intensity projection (MIP) map with respect to time (i.e., from the paths used by the tagged objects). Typically, Figure 7.3(a) shows the MIP map of a sequence made of 300 images corresponding to 10 minutes. This simple method allows us to select a subset of paths mainly used for the intracellular trafficking, leading to a network with low complexity; this approach has been successfully used for the construction of kymograms [6]. However, as shown in Figure 7.3(a), all the paths are not complete, especially if the sequence duration is too short. The gaps are then filled in by using a painting software and ad hoc image processing tools. Furthermore, the positions of the roads are extracted from the network image using the *unbiased line detection* algorithm described in [15]. Finally, each road is described by its length, its width, and its origin and destination nodes. Note that the network could also be fluorescently tagged, but the resulting network is too complex and individual microtubules cannot be easily extracted at the desired spatial resolution.

Selection of Origin-Destination Pairs

Once the network has been computed, the expert needs to specify the origin and destination nodes on the network. Since the role and function of end regions are

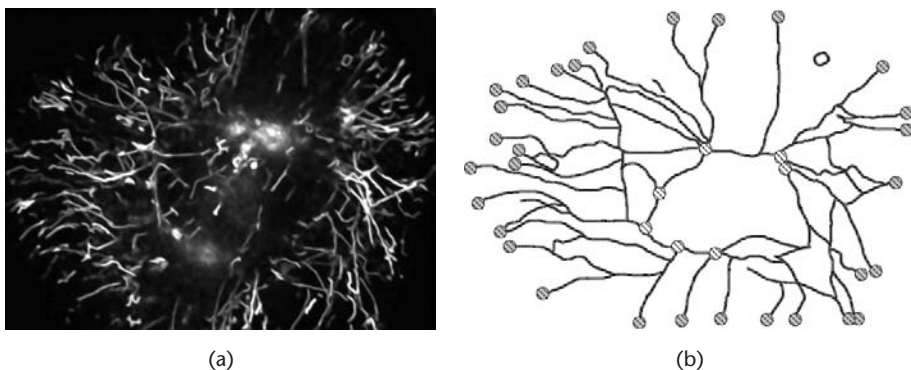


Figure 7.3 (a) Maximum intensity projection map computed from an image sequence. The paths used by the vesicles appear as bright filaments. The maximum intensity projection map has been simplified using the method described in [26]. (b) Representation of a realistic synthetic network. This network is based on a maximum intensity projection map shown in (a) and has been manually simplified.

partially unknown, a node can be labeled as an origin and a destination node, while the other nodes represent the intersection points of the network and are only used for routing. In Figure 7.3(b), the origin and destination nodes have been manually selected by the expert. The destination nodes are represented by full disks and correspond to end points while the origin nodes corresponding to the membrane of the Golgi apparatus appear as striped disks. In this simulation, vesicles are going only from the Golgi to the end points located at the periphery of the cell. Thus, the retrograde transport from end point to the Golgi is prohibited and assumed to be inhibited by biochemical alterations. Note that origin-destination pair maps are important cues in image sequence analysis, also called birth/death maps in [13].

Path Computation

In our approach, a path is defined as the minimal path between the origin and the destination nodes and is computed using the Dijkstra algorithm [16]. In that case, the weight associated with each edge can be defined as a function of the length of the corresponding road (other parameters can also be considered: speed associated with edges, number of vesicles on each edge, and so on). Finally, the vesicles are moved along the estimated roads with velocities given by the speed limit of the roads. At each time step, the vesicle is then displaced along the microtubule with a distance proportional to the adaptive velocity.

Photometric Rendering

Vesicles are superimposed against the background and are represented by anisotropic Gaussian blobs with variances related to the spot size ranging from 60 nm to 150 nm. The size of the vesicles in the image is then close to the pixel size. In addition, the covariance matrix of the anisotropic Gaussian blob is a function of the displacement direction (aligned with the microtubule direction), and the ellipticity is a function of the velocity. Finally, split-and-merge processes of several vesicles occur in real image sequences. These processes form rods, also further considered as a unique object since the merged blobs move along the same microtubule.

7.2.3 Example

In this experiment, we propose to use a real image sequence to simulate a sequence with similar photometric and dynamical contents. This requires the estimation of the model parameters from the acquired image sequence (see Sections 7.3 and 7.4).

We propose to use the sequence shown in Figure 7.4(a) that represents vesicles moving from the Golgi apparatus to the endoplasmic reticulum. Parameters of the dynamical background are first estimated as it will be described in Section 7.3. The two corresponding 2-D maps $\{a_i\}$ and $\{b_i\}$ are, respectively, shown in Figure 7.4(e, f). Given these maps, the background is subtracted from the original image to obtain the sequence of residuals shown in Figure 7.4(g), which is a noisy representation of moving blobs. The main paths used by vesicles during the 150 frames of the real sequence can be observed on the maximum intensity projection

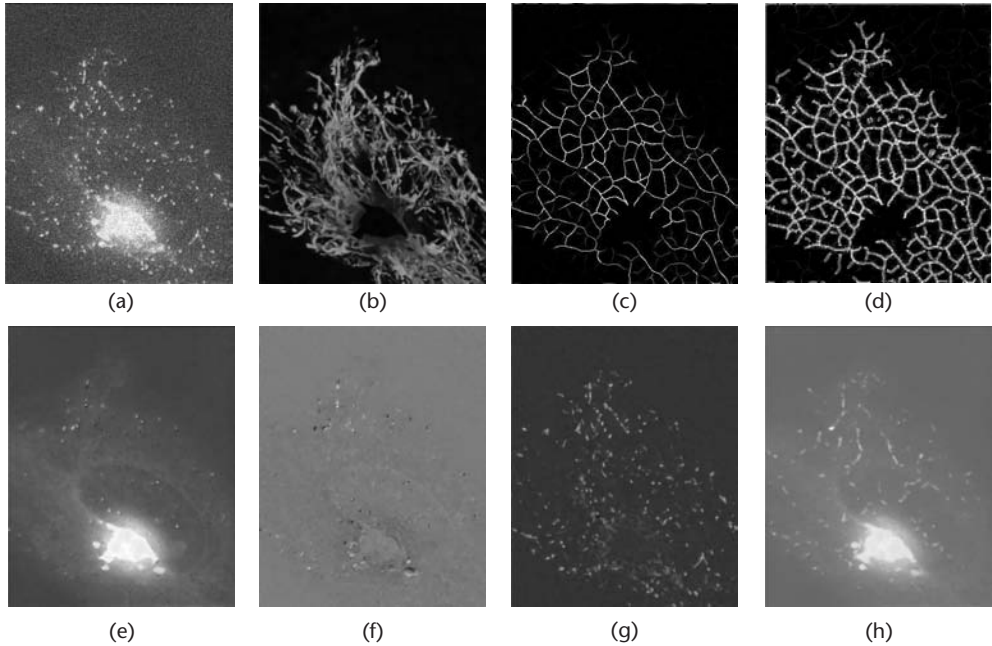


Figure 7.4 Simulation of a microscopy image sequence from a real image sequence. (a) One frame of the maximum intensity projection sequence *wrt* z axis (depth) computed from an original 3-D+time image sequence; (b) maximum intensity projection 2-D map *wrt* time t ; (c) results of steerable filtering; (d) results of the unbiased line detector; (e) map $\{a_i\}$; (f) map $\{b_i\}$; (g) residual map; and (h) noise-free image reconstruction from estimated parameters.

map in the time direction, for which the residuals are shown in Figure 7.4(b). We can enhance the maximum intensity projection map using optimal steerable filters [17] (Figure 7.4(c)). The *unbiased line detection* algorithm [15] is also applied to the enhanced image for estimating the positions of the roads shown in Figure 7.4(d). Finally 150 vesicles are moved given the estimated network. The velocities of the vesicles are tuned so that the simulated sequence is visually similar to the original input sequence.

7.3 Background Estimation in Video-Microscopy

In this section, we describe a method for estimating the parameters of the background model defined by (7.1). We start by considering the pixel-wise estimation of the parameters (a_i, b_i) for each spatial position p_i . We propose then a method for taking into account spatial correlations to derive two *regularized* maps $\{a_i\}$ and $\{b_i\}$.

7.3.1 Pixel-Wise Estimation

First, let us consider the estimation of parameters a_i and b_i for a single temporal 1-D signal. Note that the proposed estimation procedure must be very fast to

process each temporal signal, since it is applied to a $3D+time$ image sequence (several millions of voxels). Besides, as shown in Figure 7.2, vesicles may have a stochastic behavior and stop for a long time. Consequently, temporal signals cannot be easily classified, and prior motion detection cannot be used to extract the moving objects from the background. In the proposed approach, the estimation of the dynamical background will be then based on image intensity. Also, since the background is masked by moving vesicles viewed as outliers, we will also resort to a robust estimation framework, as explained in the next section.

Parameters a_i and b_i in (7.1) are estimated by minimizing a robust error function defined by $E(a_i, b_i) = \sum_{t=1}^n \rho(f_i(t) - (a_i + b_i t))$, where n is the number of samples in the 1-D signal, and $\rho(\cdot)$ is a robust function. A local minimum of $E(a_i, b_i)$ is commonly obtained by using the iteratively reweighted least squares (IRLS) procedure.

The choice of the robust function ρ is usually guided by the noise probability density function [18]. In our case, the overall noise is the sum of two components $u_i(t)$ and $\varepsilon_i(t)$. Since $u_i(t)$ usually takes high positive values (vesicles appear as bright blobs in the image), we decide to choose an asymmetric robust function (Leclerc estimator [19,20]) plotted in Figure 7.5(a) and defined as

$$\rho(z) = \begin{cases} 1 - \exp\left(-\frac{z^2}{\lambda^2 \sigma_1^2}\right) & \text{if } z \leq 0, \\ 1 - \exp\left(-\frac{z^2}{\lambda^2 \sigma_2^2}\right) & \text{otherwise,} \end{cases} \quad (7.2)$$

where σ_1 and σ_2 are two scale parameters and λ acts as a threshold chosen in the range [1,3]. This threshold is relative to the point where the derivative of the $\rho'(\cdot)$ -function is zero (see [21]). The scale factor σ_2 can be estimated by applying a robust least-trimmed squares (LTS) estimator to the *pseudo-residuals* (see [22]) defined as $s_i(t) = (f_i(t+1) - f_i(t))/\sqrt{2}$, where the coefficient $1/\sqrt{2}$ ensures that $\mathbb{E}[(s_i(t))^2] = \mathbb{E}[(f_i(t))^2]$. The scale factor σ_1 is estimated by using the variance of the residuals given by the least-mean-squares estimator and obtained at the initialization of the estimated procedure. Let us point out that in regions where there are no moving vesicles, σ_1 and σ_2 are found to be almost equal.

As a matter of fact, even though the proposed estimator is slightly biased [20], simulations proved that the L_2 risk of the estimator is smaller with an asymmetric cost function when data are corrupted by an additive positive signal. Finally, as shown in Figure 7.5(b), the proposed estimator is able to deal with heavily contaminated data and outperforms the symmetric Leclerc M-estimator.

However, this point-wise procedure is not sufficient to accurately estimate the background parameters for all the pixels/voxels. For improving estimations quality, we propose exploiting the spatial correlation between the parameters a_i and b_i .

7.3.2 Spatial Coherence for Background Estimation

Spatial regularization can be accomplished by adopting the *bias-variance tradeoff* framework already described in [23–26]. Instead of using a single temporal signal

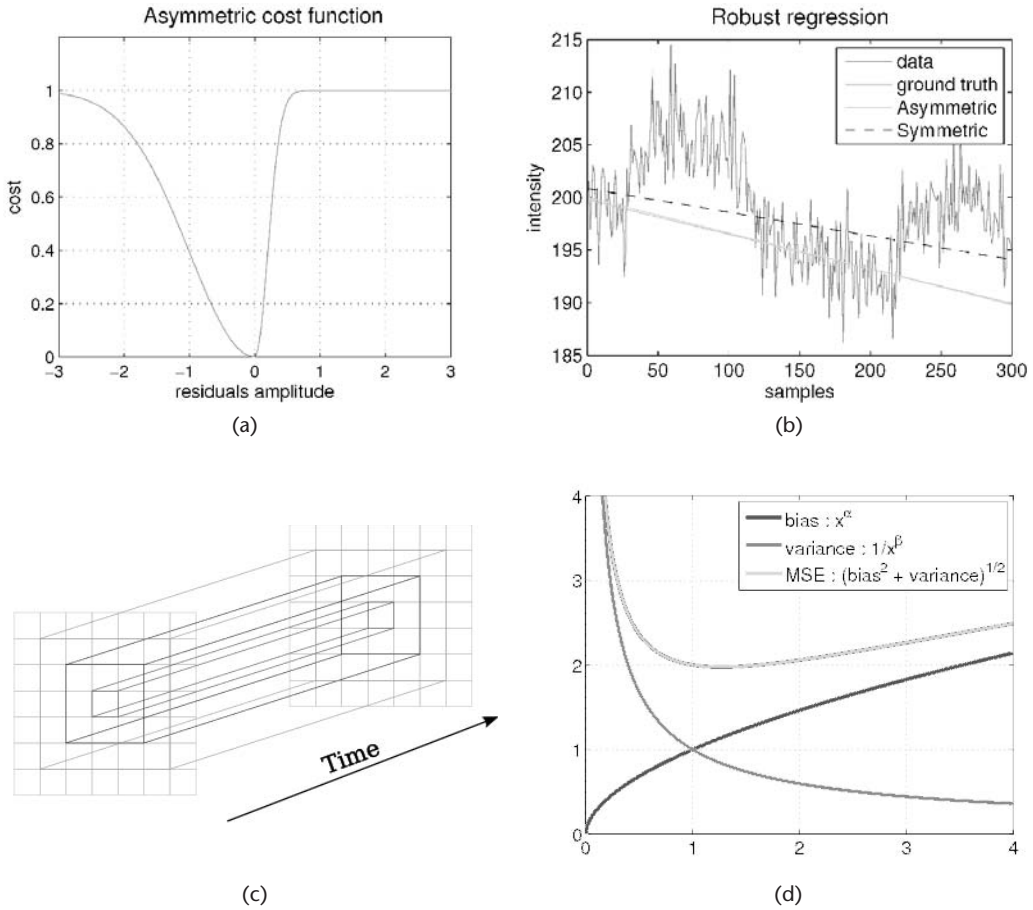


Figure 7.5 (a) Asymmetric Leclerc robust function. (b) Regression using an asymmetric and symmetric robust Leclerc function. The asymmetric estimator fits perfectly the ground truth while the symmetric function provides biased results (dotted line). (c) Set of nested tubes $\{\mathcal{T}_{i,k}\}_{k=1,\dots,3}$. (d) Bias-variance trade-off principle. When the tube diameter increases, the bias increases and the variance decreases. The optimum is achieved when the bias and the variance are of the same order.

for each pixel p_i to estimate a_i and b_i , a set of temporal 1-D signals is first collected in a spatial neighborhood of pixel p_i . A set of nested space-time tubes is considered by taking the pixels in a growing spatial square neighborhood of p_i (see Figure 7.5(c)). Each tube $\mathcal{T}_{i,k}$ at p_i is parameterized by its diameter $\phi_{i,k}$, where $k \in [1, \dots, K]$ denotes the iteration of the procedure.

To select the optimal diameter of the space-time tube at pixel p_i , the point-wise L_2 risk $\mathbb{E}[(\hat{\theta}_i - \theta_i)^2]$ (decomposed into two parts: squared bias and variance) of the estimator is minimized, where $\theta_i = (a_i, b_i)$ denotes the true value, and $\hat{\theta}_i$ is the corresponding estimator at pixel p_i . As shown in Figure 7.5(d), while the diameter $\phi_{i,k}$ increases with k , the bias increases too. This can be explained by the fact that the data cannot be described any longer by a unique parametric model. In contrast, by taking more data points, the variance decreases. This behavior, also

called *bias-variance tradeoff*, is exploited to detect the minimum of the point-wise L_2 risk, which is nearly equal to twice the variance [23] (see Figure 7.5(d)).

For each diameter $\phi_{i,k}$, new estimates of the background model parameters $\hat{\theta}_{i,k}$ and the associated covariance matrix $\hat{C}_{i,k}$ (as proposed in [18]) are computed with the procedure described in Section 7.3.1, but by using all the data taken in the considered spatial neighborhood. Furthermore, it can be shown that the *bias-variance tradeoff* can be expressed with the following statistical test [26]:

$$\frac{n-2+1}{2n} \left(\hat{\theta}_{i,k} - \hat{\theta}_{i,k'} \right)^T \hat{C}_{i,k'}^{-1} \left(\hat{\theta}_{i,k} - \hat{\theta}_{i,k'} \right) < \eta \quad (7.3)$$

for all $1 \leq k' < k$, where the threshold η is defined as a quantile of a Fisher distribution of parameters 2 and $n-2-1$, since we use an estimator of the covariance matrix. While this inequality is satisfied, the diameter of the tube is increased and the estimation process is continued.

7.3.3 Example

We now describe an experiment that demonstrates the performance of the estimation method. For this purpose, we use the real image sequence shown in Figure 7.4(a). The estimated maps $\{\hat{a}_i\}$ and $\{\hat{b}_i\}$ are, respectively, shown in Figure 7.4(e, f). The map $\{\hat{a}_i\}$ related to the static component of the background model reveals several interesting locations in the cell. The very bright region is associated to the Golgi apparatus, while the bean-shaped darker region indicates the location of the nucleus. Finally, Figure 7.4(g) shows the residual map containing only the vesicles, appearing as small blobs in the foreground of the image sequence. Next section deals with the estimation of the model parameters describing the foreground.

7.4 Foreground Analysis: Network Tomography

We propose here a method to estimate flows between origin-destination (OD) pairs. If these flows are known, simulation can be performed as described in Section 7.2. This approach was applied to the analysis of road trafficking [27], and more recently to communication networks [28].

Usual approaches for traffic analysis in video-microscopy aim at tracking each object. The most commonly used tracking concept is the connexionist approach [29, 30] consisting of detecting particles independently in each frame and then linking the detected objects over time. In the case of Rab6 analysis, temporal sampling is quite low compared to the speed of the numerous vesicles. Then, the correspondence between the detected objects and their entire trajectories (data association) is very hard to compute. Recent data association combined with sophisticated particle filtering techniques [31], fast marching methods [32], or graph theory-based methods [10, 33] have been successfully applied and solve the tracking problem in these difficult conditions. In this chapter, we propose an alternative framework also consistent with traffic modeling. Note that the OD flow problem is also related to the extraction of kymograms in video-microscopy image

sequence [6] in the sense that it also uses the microtubule network as a priori information.

In this section, we first introduce the concept of network tomography (NT). Then, we propose an original approach to measure activities on the network edges, which amounts to counting vesicles in regions, avoiding tracking, and motion estimation. Finally, we present an optimization framework to estimate the origin-destination flows from these measurements.

7.4.1 Network Tomography Principle

We now introduce the principle of NT and its application to video-microscopy trafficking. In Section 7.2, a network model has been introduced to describe the foreground in the image sequences. In this model, the graph associated with the microtubule network is composed of vertices associated with crossings or origin and destination nodes, and edges associated to “roads” used by the vesicles. To estimate flows of objects, a straightforward approach would be to measure the activity on the roads. However, this requires an accurate localization of the roads and reliable detection of the vesicles which are both known to be hard problems in computer vision. In what follows, we consider a network with a limited number of nodes (to indicate cell regions obtained by image partitioning).

7.4.1.1 Partitioning the Cell Region

The maximum intensity projection (MIP) map in the direction of time axis is a precious key for partitioning the imaged region. We assume that the likely regions of origin or destination correspond to brighter spots in the MIP map because vesicles are temporally stocked in these areas. For illustration, the MIP map extracted from the image sequence shown in Figure 7.4(a) is given in Figure 7.4(g). A possible image partitioning consists of arbitrarily dividing the MIP image into Voronoi cells given a set of labeled regions obtained automatically or supplied by the expert biologist if required, as proposed in [34]. A partition for the cell observed in the image sequence of Figure 7.4(a) is typically illustrated in Figure 7.6(a), where the centers are represented as crosses and the different regions appear in gray levels, while the MIP map is depicted in the background. In practical imaging, the Voronoi diagram is computed using the *qhull* library [35].

Note that the Voronoi diagram can be described by an adjacency graph (Figure 7.6(b)), which is consistent with the NT concept used for tracking. The different Voronoi cells represent the set of vertices V , while the boundaries between the cells represent the set of edges E , so the graph $G(E, V)$ is wholly defined. Finally, we introduce two edges in the graph between two neighboring cells for bidirectional trafficking.

7.4.1.2 Network Tomography Concept

We present more formally the estimation of the OD flows on the designed network. The graph G is composed of n vertices and r edges. An *origin/destination pair* is a *couple* of vertices in the graph linking an *origin* vertex to a *destination* vertex. So,

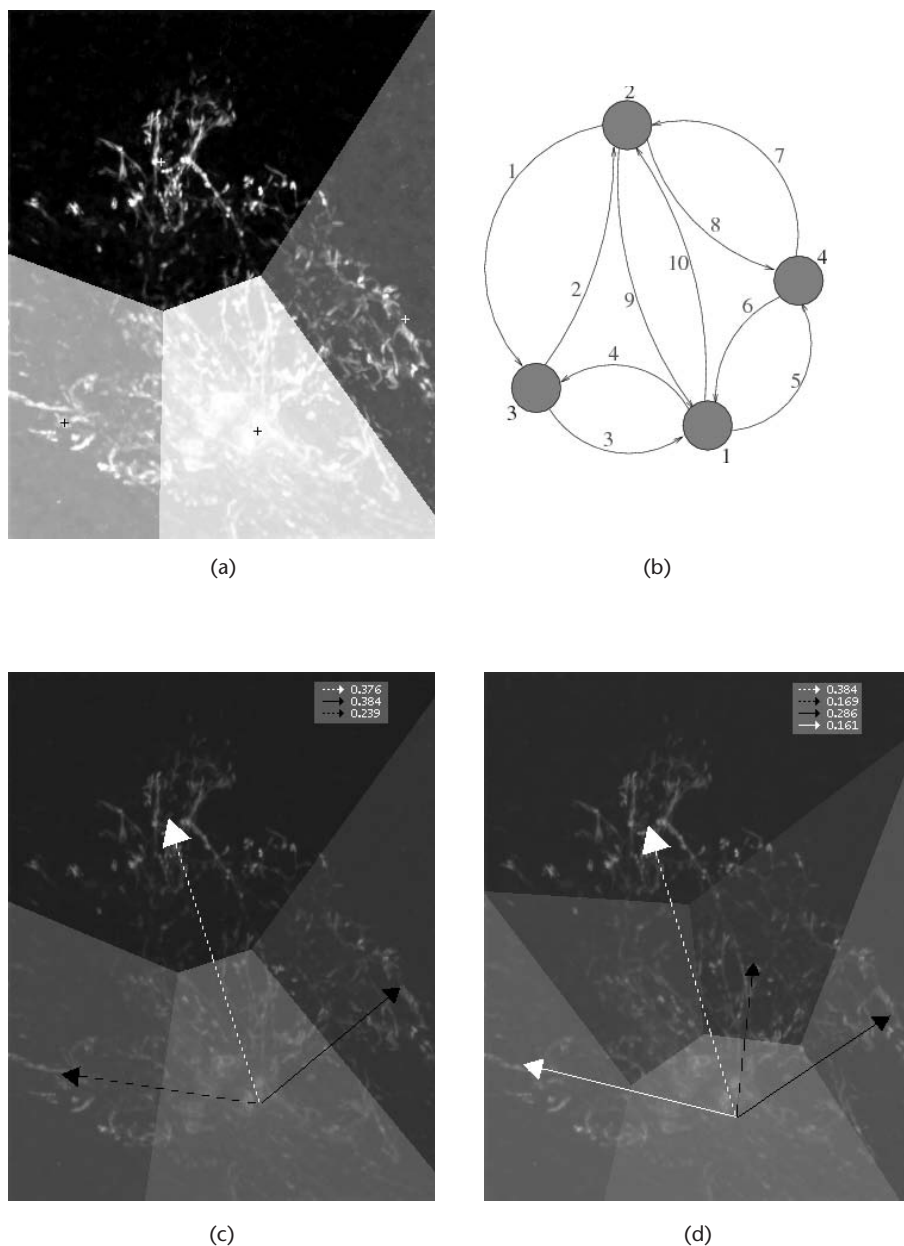


Figure 7.6 (a) Partition of the image sequence shown in Figure 7.4(a) by using a Voronoi decomposition. The different regions appear in gray levels, their centers appear as crosses, and the MIP map is depicted in the background; (b) the corresponding graph; and (c) and (d) results obtained by applying the NT-based approach on the sequence of the Figure 7.4(a). The arrows represent the estimated OD pairs, and the corresponding numbers at the top right represent traffic proportions. For these two experiments, the region at the bottom is imposed to be an origin region.

Table 7.1 Part of Matrix **A** Corresponding to the Graph Shown in Figure 7.6(b)

OD Pairs	Edges									
	1	2	3	4	5	6	7	8	9	10
1 → 2	0	0	0	0	0	0	0	0	0	1
1 → 3	0	0	0	1	0	0	0	0	0	0
1 → 4	0	0	0	0	1	0	0	0	0	0
2 → 1	0	0	0	0	0	0	0	0	1	0
2 → 3	1	0	0	0	0	0	0	0	0	0
2 → 4	0	0	0	0	0	0	0	1	0	0
3 → 1	0	0	1	0	0	0	0	0	0	0
3 → 2	0	1	0	0	0	0	0	0	0	0
3 → 4	0	0	1	0	1	0	0	0	0	0
...					...					

the set of all possible OD pairs is composed of $c = n(n - 1)$ elements. Given the number of objects detected as going from one vertex to a neighbor vertex in the graph, the goal consists of estimating how many vesicles use each OD pair, by linking OD pairs with edges, thanks to a routing procedure. This problem is then similar to determining the source-destination trafficking based on link measurements in computer networks [28].

Let $X_{j,t}$, $j = 1, \dots, c$ be the number of “transmitted” vesicles on the OD pair j at time t . The measurements $\mathbf{Y}_t = (Y_{1,t}, \dots, Y_{r,t})^T$ are the number of vesicles that pass from one vertex to another vertex at time t . In this traffic flow problem, we then assume the following model:

$$\mathbf{Y}_t = \mathbf{A}\mathbf{X}_t \quad (7.4)$$

where $\mathbf{X}_t = (x_{1,t}, \dots, x_{c,t})^T$, and \mathbf{A} denotes an $r \times c$ routing matrix, which has binary elements $A_{ij} = 1$ if edge i is in the path for the OD pair j , and 0 otherwise. The path between two vertices in the graph is defined as the shortest path between these two vertices. For illustration, if we consider the simple example shown in Figure 7.6(b), some rows of the matrix \mathbf{A} are presented in Table 7.1. The aim is to estimate \mathbf{X}_t given \mathbf{A} , but in image sequences, the counting analysis data \mathbf{Y}_t are not available and must be carefully computed. We address this problem in the next section.

7.4.2 Measurements

The application of NT requires knowing exactly how many vesicles are moving from one Voronoi cell to another one at each time step. Our idea is to compute the difference of the number of vesicles observed at two consecutive time steps in each neighboring region and then to infer the exact number of vesicles that crosses each common boundary. Moreover, we assume that the level of fluorescence is proportional to the number of objects at each pixel. So the difference of image intensity between two time steps represents the difference of the number of objects in each region. Preliminary, the background corresponding to the Golgi Apparatus

Table 7.2 Definition of Matrix \mathbf{M} Corresponding to the Graph Shown in Figure 7.6(b)

Vertices	Edges									
	1	2	3	4	5	6	7	8	9	10
1	0	0	1	-1	-1	1	0	0	1	1
2	-1	1	0	0	0	0	1	-1	-1	-1
3	1	-1	-1	1	0	0	0	0	0	0
4	0	0	0	0	1	-1	-1	1	0	0

and the cytosol is removed using the preprocessing algorithm, as explained in Section 7.3. We illustrate this idea using a simple example.

We consider the fluorescence exchanges at vertex 1 in the graph shown in Figure 7.6(b). Let $Z_{v,t}$ be the total amount of fluorescence at vertex v and time t , and let $Y_{e,t}$ be the level of fluorescence to be determined on edge e at time t :

$$Z_{1,t+1} - Z_{1,t} = Y_{3,t+1} - Y_{4,t+1} + Y_{6,t+1} - Y_{5,t+1} + Y_{9,t+1} - Y_{10,t+1}$$

This equation can be extended to all vertices: let $\Delta\mathbf{Z}$ be the $n \times t$ matrix corresponding to the difference of fluorescence in each region between two consecutive time steps, with n the number of regions and t the number of images in the sequence. Let \mathbf{Y} be the $r \times t$ matrix representing the level of fluorescence that fluctuates from one region to another at each time, with r denoting the number of edges. We define \mathbf{M} as the so-called “neighborhood $n \times r$ matrix” composed of ternary elements $m = \{-1, 0, 1\}$ that links the regions according to the neighborhood relationships. For example, in the graph of Figure 7.6(b), \mathbf{M} is defined as shown in Table 7.2. Then, we have the linear equation:

$$\Delta\mathbf{Z} = \mathbf{M}\mathbf{Y} \quad (7.5)$$

Our aim is to estimate \mathbf{Y} with $r > n$ given $\Delta\mathbf{Z}$, to solve an *under-constrained* problem. Additional constraints are necessary for solving (7.5). First, we assume that all the components of \mathbf{Y} are positive since the edges are unidirectional. In addition, the $\Delta\mathbf{Z}$ rows are assumed to be independent and identically distributed (i.i.d.), and Gaussian distributed. This leads to the following optimization problem:

$$\hat{\mathbf{Y}} = \min_{\mathbf{Y}} \|\Delta\mathbf{Z} - \mathbf{M}\mathbf{Y}\|^2 \text{ subject to } \mathbf{Y} \geq 0$$

solved by a nonnegative least square algorithm. The estimated measurements are further used for NT.

7.4.3 Problem Optimization

Once the data are estimated, we have to estimate \mathbf{X}_t from (7.4). The inherent randomness of the measurements motivates the adoption of a statistical approach.

7.4.3.1 General Case

We reasonably assume that the whole traffic is temporally distributed as a Poisson process—(i.e., $\mathbf{X}_{j,t} \sim \text{Poisson}(\lambda_j)$). Then, the number c is greater than r , and the problem is under constrained. Additional constraints are necessary for solving this *inverse problem*. First, in [28], the author proposed introducing constraints related to the assumption that the traffic is temporally Poisson distributed. The NT method amounts then to estimating the values λ_j given the additional set of equations corresponding to temporal averages:

$$\begin{cases} \bar{Y}_i = \sum_{k=1}^c A_{i,k} \lambda_k, & i = 1, \dots, r \\ \text{cov}(Y_i, Y_{i'}) = \sum_{k=1}^c A_{i,k} A_{i',k} \lambda_k, & 1 \leq i \leq i' \leq r \end{cases}$$

This set of equations gives a system of $r(r+3)/2$ linear equations that forms an overconstrained problem that can be better solved with the conditions $\lambda_i \geq 0$. Moreover, in this study, the aim is not to obtain the number of vesicles that utilize each path, but to estimate the proportions of vesicles on each path. Hence, unlike previous methods [28,34,36], we impose the condition $\sum_{i=1}^c \lambda_i = 1$ as an additional constraint. The previous system can be written more compactly as:

$$\begin{pmatrix} \bar{\mathbf{Y}} \\ \mathbf{S} \end{pmatrix} = \begin{pmatrix} \mathbf{A} \\ \mathbf{B} \end{pmatrix} \Lambda \quad (7.6)$$

where $\Lambda = (\lambda_1, \dots, \lambda_c)^T$ contains the temporal mean of the traffic flow, $\mathbf{S} = \{\text{cov}(Y_i, Y_{i'})\}$ is the sample covariance matrix rewritten as a vector of length $r(r+1)/2$, and \mathbf{B} is an $(r(r+1)/2) \times c$ matrix with the (i, i') th row of \mathbf{B} being the element-wise product of row i and row i' of the matrix \mathbf{A} .

The system can be solved using the estimation-maximization (EM) method [28, 36] or the convex-projection algorithms [34]. In our case, we adapt a nonnegative mean square estimation that also provides a simple and reliable way to estimate the OD traffic $\hat{\Lambda}$. Note that a review of existing methods is proposed in [37].

7.4.3.2 More Constraints and A Priori Knowledge

When the expert specifies the origin or destination regions, the problem is better constrained and the solution is expected to be more relevant. If we assume that the origins or destinations are known, this can be casted into additional hard constraints. Typically, if the Voronoi cell r is the single origin region to be considered, then all the OD pairs involving other origin cells except r should be discarded. Hence, let \mathcal{R} be the set of OD pairs for which r is the origin vertex. Then, if \mathcal{O} denotes the set of all OD pairs, \mathbf{A} can be modified as follows:

$$\mathbf{A}(:, \mathcal{O} \setminus \mathcal{A}) = 0$$

with $\mathbf{A}(:, \mathcal{O} \setminus \mathcal{A}) = \{\mathbf{A}(1, \mathcal{O} \setminus \mathcal{A}); \mathbf{A}(2, \mathcal{O} \setminus \mathcal{A}); \dots; \mathbf{A}(r, \mathcal{O} \setminus \mathcal{A})\}$. The same modeling can be applied for imposing additional origin or destination regions. This

demonstrates the flexibility of the approach, adapted to situations when prior knowledge is required.

7.4.4 Experiments

In this section, we propose two experiments to demonstrate the ability of the NT-based approach for a real image sequence. All these experiments are tested by considering the sequence shown in Figure 7.4(a). This sequence is composed of 150 images extracted from a fast 4-D deconvolution microscopy (wide-field) process [6]. First, the background has been removed during a preprocessing step. The estimated results are reported in Figure 7.6(c, d). In these figures, the Voronoi cells are in gray levels, while the MIP map is shown in the background by transparency. The different estimated OD pairs appear as arrows, and the corresponding numbers at the right top of the figures are the estimated proportions of moving vesicles for each OD pair.

A first experience was carried out with a crude segmentation (Figure 7.6(c)). According to the expert biologists, the vesicles are moving from the Golgi Apparatus (the region at the bottom) to end points located at the periphery of the cell (corresponding to the three other regions)—that is why we impose the region at the bottom to be the origin Voronoi cell. The results obtained with this additional hard constraint correspond to trafficking from the Golgi Apparatus to the end points. In that case, the traffic tends to be a little denser in the regions at the top and on the right than in the region on the left.

In another experiment corresponding to another partition of the image shown in Figure 7.6(d), two Voronoi cells are added between the origin cell and the destination cells. The Voronoi cell located at the bottom is still constrained to be the origin cell. With this partitioning, another destination cell appears at the top right of the compartment. This is not in contradiction with the expert biologists since this region is located on the periphery of the cell. We observe that the amount of traffic that had the right Voronoi cell for destination in the previous experiment is divided into the two destination cells on the right of the compartment for this experiment.

7.5 Conclusions

We have described an original framework for the analysis of the dynamical content of fluorescence video-microscopy dedicated to the intracellular membrane trafficking. We have briefly introduced the biological context and fluorescence video-microscopy, and presented a data-based modeling for the intracellular trafficking. The proposed model is parametric with few degrees of freedom and relies on the separation between background/foreground. It provides a statistical description of the events observed in the cell. This modeling can be used for image simulation; the input parameters are either specified by the user or estimated beforehand from real image sequences. In the latter case, a point-wise adaptive estimation is presented for estimating the parameters related to the background of the sequence. Then,

network tomography is used to recover from the sequence the origin-destination probabilities associated to the particles. Measurements are a critical point in this framework, and an original method is described to avoid motion estimation and tracking in noisy video-microscopy.

Even though these preliminary results are encouraging, this new estimation/simulation approach still needs further development. We hope that it will help to better understand the mechanisms involved in the intracellular traffic.

References

- [1] Chowdhury, D., L. Santen, and A. Schadschneider, "Statistical Physics of Vehicular Traffic and Some Related Systems," *Physics Reports*, Vol. 329, 2000, p. 199.
- [2] Helbing, D., "Traffic and Related Self-Driven Many-Particle Systems," *Review of Modern Physics*, Vol. 73, October 2001, pp. 1067-1141.
- [3] Soatto, S., G. Doretto, and Y. N. Wu, "Dynamic Textures," *Proc. of ICCV'2001*, Vol. 2, Vancouver, Canada, July 2001, pp. 439-446.
- [4] Sibarita, J.-B., H. Magnin, and J. R. De Mey, "Ultra-Fast 4D Microscopy and High Throughput Distributed Deconvolution," *Proc. of IEEE ISBI'2002*, Washington, D.C., June 2002, pp. 769-772.
- [5] Zhang, B., J. Enninga, J.-C. Olivo-Marin, and C. Zimmer, "Automated Super-Resolution Detection of Fluorescent Rods in 2D," *Proc. of IEEE ISBI'2006*, Washington, D.C., April 2006, pp. 1296-1299.
- [6] Sibarita, J.-B., V. Racine, and J. Salamero, "Quantification of Membrane Trafficking on a 3D Cytoskeleton Network in Living Cells," *Proc. of IEEE ISBI'2006*, Washington, D.C., April 2006.
- [7] Gibbons, F., J. Chauwin, M. Desposito, and J. José, "A Dynamical Model of Kinesin-Microtubule Motility Assays," *Biophysical Journal*, Vol. 80, June 2001, pp. 2515-2526.
- [8] Nédélec, F., "Computer Simulations Reveal Motor Properties Generating Stable Antiparallel Microtubule Interactions," *Journal of Cell Biology*, Vol. 158, September 2001, pp. 1005-1015.
- [9] Genovesio, A., T. Liedl, V. Emiliani, W. J. Parak, M. Coppey-Moisan, and J.-C. Olivo-Marin, "Multiple Particle Tracking in 3D+t Microscopy: Method and Application to the Tracking of Endocytosed Quantum Dots," *IEEE Trans. on IP*, Vol. 15, May 2006, pp. 1062-1070.
- [10] Racine, V., A. Hertzog, J. Jouaneau, J. Salamero, C. Kervrann, and J.-B. Sibarita, "Multiple Target Tracking of 3D Fluorescent Objects Based on Simulated Annealing," *Proc. of IEEE ISBI'2006*, Washington, D.C., April 2006.
- [11] Portilla, J., V. Strela, M. Wainwright, and E. Simoncelli, "Image Denoising Using Scale Mixtures of Gaussians in the Wavelet Domain," *IEEE Trans. on IP*, Vol. 12, November 2003, pp. 1338-1351.
- [12] Barron, J. L., D. J. Fleet, and S. S. Beauchemin, "Performance of Optical Flow Techniques," *IJCV*, Vol. 12, January 1994, pp. 43-77.
- [13] Wang, Y., and S. C. Zhu, "Modeling Textured Motion: Particle, Wave and Sketch," *Proc. of ICCV 2003*, October 2003.
- [14] Surrey, T., F. Nédélec, S. Leibler, and E. Karenti, "Physical Properties Determining Self-Organization of Motors and Microtubules," *Science*, Vol. 292, May 2001, pp. 1167-1171.
- [15] Steger, C., "An Unbiased Detector of Curvilinear Structures," *IEEE Trans. on PAMI*, Vol. 20, February 1998, pp. 113-125.

- [16] Dijkstra, E. W., "A Note on Two Problems in Connexion with Graphs," *Numerische Mathematik*, Vol. 1, December 1959, pp. 269-271.
- [17] Jacob, M., and M. Unser, "Design of Steerable Filters for Feature Detection Using Canny-Like Criterion," *IEEE Trans. on PAMI*, Vol. 26, August 2004, pp. 1007-1019.
- [18] Ieng, S.-S., J.-P. Tarel, and P. Charbonnier, "Evaluation of Robust Fitting Based Detection," *Proc. of ECCV'2004*, Vol. 2, Prague, Czech Republic, May 2004, pp. 341-352.
- [19] Allende, H., A. Frery, J. Galbiati, and L. Pizarro, "M-Estimator with Asymmetric Influence Function: The \mathcal{G}_a^0 Distribution Case," *Journal of Statistical Computation and Simulation*, Vol. 76, November 2006, pp. 941-946.
- [20] Ruckstuhl, A., M. Jacobson, R. Field, and J. Dodd, "Baseline Subtraction Using Robust Local Regression Estimation," *Journal of Quantitative Spectroscopy and Radiative Transfer*, Vol. 68, January 2001, pp. 179-193.
- [21] Black, M., G. Sapiro, D. Marimont, and D. Heeger, "Robust Anisotropic Diffusion," *IEEE Trans. on IP*, Vol. 7, March 1998, pp. 421-432.
- [22] Gasser, T., L. Sroka, and C. Jennen-Steinmetz, "Residual Variance and Residual Pattern in Nonlinear Regression," *Biometrika*, Vol. 73, 1986, pp. 625-633.
- [23] Lepski, O., "Asymptotically Minimax Adaptive Estimation 1: Upper Bounds," *SIAM Journal Theory of Probability and Application*, Vol. 36, No. 4, 1991, pp. 654-659.
- [24] Maurizot, M., P. Bouthemy, B. Delyon, A. Iouditski, and J.-M. Odobez, "Determination of Singular Points in 2D Deformable Flow Fields," *Proc. of ICIP'1995*, Vol. 3, Washington, D.C., October 1995, pp. 488-491.
- [25] Ercole, C., A. Foi, V. Katkovnik, and K. Egiazarian, "Spatio-Temporal Pointwise Adaptive Denoising in Video: 3D Non Parametric Approach," *Proc. of 1st International Workshop on Video Processing and Quality Metrics for Consumer Electronics, VPQM 2005*, Scottsdale, AZ, January 2005.
- [26] Kervrann, C., and J. Boulanger, "Optimal Spatial Adaptation for Patch-Based Image Denoising," *IEEE Trans. on IP*, Vol. 15, No. 10, 2006, pp. 2866-2878.
- [27] Cascetta, E., and S. Nguyen, "A Unified Framework for Estimating or Updating Origin/Destination Matrices from Traffic Counts," *Transportation Research*, Vol. 22, No. 6, 1988, pp. 437-455.
- [28] Vardi, Y., "Network Tomography: Estimation Source-Destination Traffic Intensities from Link Data," *Journal of the American Statistical Association*, Vol. 91, March 1996, pp. 365-377.
- [29] Anderson, C., G. Georgiou, I. Morrison, G. Stevenson, and R. Cherry, "Tracking of Cell Surface Receptors by Fluorescence Digital Imaging Microscopy Using a Charged-Coupled Device Camera. Low-Density Lipoprotein and Influenza Virus Receptor Mobility at 4 Degrees C," *Journal of Cell Science*, Vol. 101, 1992, pp. 415-425.
- [30] Sbalzarini, I., and P. Koumoutsakos, "Feature Point Tracking and Trajectory Analysis for Video Imaging in Cell Biology," *Journal of Structural Biology*, Vol. 151, 2005, pp. 182-195.
- [31] Smal, I., W. Niessen, and E. Meijering, "Advanced Particle Filtering for Multiple Object Tracking in Dynamic Fluorescence Microscopy Images," *Proc. of IEEE ISBI 2007*, Arlington, VA, April 2007, pp. 1048-1051.
- [32] Bonneau, S., M. Dahan, and L. D. Cohen, "Tracking Single Quantum Dots in Live Cells with Minimal Paths," *Proc. of IEEE CVPR'2005*, Vol. 3, San Diego, CA, June 2005, pp. 141-149.
- [33] Thomann, D., J. Dorn, P. Sorger, and G. Danuser, "Automatic Fluorescent Tag Localization II: Improvement in Super-Resolution by Relative Tracking," *Journal of Microscopy*, Vol. 211, September 2003, pp. 230-248.
- [34] Boyd, J. E., J. Meloche, and Y. Vardi, "Statistical Tracking in Video Traffic Surveillance," *Proc. of ICCV'99*, Vol. 1, Kerkyra, Greece, September 1999, pp. 163-168.

- [35] Barber, C., D. Dobkin, and H. T. Huhdanpaa, "The Quickhull Algorithm for Convex Hulls," *ACM Transactions on Mathematical Software*, Vol. 22, December 1996, pp. 469-483.
- [36] Santini, S., "Analysis of Traffic Flow in Urban Areas Using Web Cameras," *Fifth IEEE Workshop on Applications of Computer Vision*, Vol. 596, 2000, pp. 140-145.
- [37] Medina, A., N. Taft, K. Salamatian, S. Bhattacharyya, and C. Diot, "Traffic Matrix Estimation: Existing Techniques and New Directions," *Proc. of Conference on Applications, Technologies, Architectures, and Protocols for Computer Communications, SIGCOMM '02*, New York, 2002, pp. 161-174.